



Technical Note

Composite Actuation and Adaptive Control for Hypersonic Reentry Vehicles: Mitigating Aerodynamic Ablation via Moving Mass-Aileron Integration

Pengxin Wei 1,* D, Peng Cui 2 and Changsheng Gao 2,3

- Heilongjiang Provincial Key Laboratory of Complex Intelligent System and Integration, School of Automation, Harbin University of Science and Technology, Harbin 150080, China
- ² Department of Aerospace Engineering, Harbin Institute of Technology, Harbin 150001, China
- National Key Laboratory of Modeling and Simulation for Complex Systems, Harbin Institute of Technology, Harbin 150001, China
- * Correspondence: weipengxin@hrbust.edu.cn

Abstract

Aerodynamic ablation of external control surfaces and structural complexity in hypersonic reentry vehicles (HRVs) pose significant challenges for maneuverability and system reliability. To address these issues, this study develops a novel bank-to-turn (BTT) control strategy integrating a single internal moving mass with differential ailerons, eliminating reliance on ablation-prone elevators/rudders while enhancing internal space utilization. A coupled 7-DOF dynamics model explicitly quantifies inertial-rolling interactions induced by the moving mass, revealing critical stability boundaries for roll maneuvers. To ensure robustness against aerodynamic uncertainties, aileron failures, and high-frequency massinduced disturbances, a dynamic inversion controller is augmented with an L1 adaptive layer decoupling estimation from control for improved disturbance rejection. Monte Carlo simulations demonstrate: (1) a 20.6% reduction in roll-tracking error (L2-norm) under combined uncertainties compared to dynamic inversion control, and (2) a 72% suppression of oscillations under aerodynamic variations. Comparative analyses confirm superior transient performance and robustness in worst-case scenarios. This work offers a practical solution for high-maneuverability hypersonic vehicles, with potential applications in reentry vehicle design and multi-actuator system optimization.

Keywords: hypersonic reentry vehicle; aerodynamic ablation mitigation; moving massaileron integration; L1 adaptive control; inertial-rolling dynamics



Academic Editor: Karim Abu Salem

Received: 26 June 2025 Revised: 13 August 2025 Accepted: 24 August 2025 Published: 28 August 2025

Citation: Wei, P.; Cui, P.; Gao, C. Composite Actuation and Adaptive Control for Hypersonic Reentry Vehicles: Mitigating Aerodynamic Ablation via Moving Mass-Aileron Integration. *Aerospace* **2025**, *12*, 773. https://doi.org/10.3390/aerospace12090773

Copyright: © 2025 by the authors. Licensee MDPI, Basel, Switzerland. This article is an open access article distributed under the terms and conditions of the Creative Commons Attribution (CC BY) license (https://creativecommons.org/licenses/by/4.0/).

1. Introduction

Hypersonic reentry vehicles (HRVs) demand precise attitude control systems capable of withstanding extreme aerodynamic heating, parametric uncertainties, and cross-channel coupling effects. Traditional control actuators—aerodynamic surfaces and reaction control systems (RCS)—face inherent limitations: elevators and rudders suffer from thermal ablation during reentry, whereas RCS implementations require substantial fuel reserves that increase system mass and complexity. Recent advances in fault-tolerant spacecraft attitude control, such as incremental optimization on SO(3) manifolds [1] and geometric sliding-mode methods [2], demonstrate remarkable resilience to actuator failures. However, these approaches encounter unique challenges in hypersonic regimes due to: millisecond-scale dynamics exceeding real-time optimization capabilities, and high-frequency flow disturbances (>10 Hz) disrupting smooth manifold convergence.

Internal moving mass control, which generates control moments by manipulating the vehicle's center of mass, has emerged as a promising alternative. This approach offers higher efficiency than aerodynamic surfaces and maintains compatibility with streamlined hypersonic shapes [3–6]. Despite the theoretical promise of moving mass control, two critical challenges hinder its practical implementation in hypersonic systems: (1) achieving multi-axis maneuverability without compromising structural simplicity, and (2) maintaining stability under inertial coupling effects.

Existing studies on moving mass control primarily focus on configurations with multiple actuators for longitudinal/lateral control [7,8] or single-mass systems for roll stabilization [9,10]. While multi-actuator designs enable versatile maneuvers, their implementation in compact HRV airframes remains impractical due to spatial constraints and increased mechanical complexity. Conversely, single-moving-mass systems, though structurally simpler, exhibit limited control authority and are susceptible to inertial coupling during aggressive maneuvers [11]. Frost and Costello [12] pioneered spin-stabilized projectile control using rotating masses but limited their analysis to subsonic regimes. Recent work by Li et al. [13] attempted to address this by integrating jet thrusters with moving masses, but introduced new complexities in fuel management and actuator coordination. Crucially, prior studies fail to resolve two interconnected challenges in composite moving mass-aileron systems: (1) high-frequency disturbance transmission from mass motion to roll dynamics, and (2) nonlinear inertia modulation during aggressive BTT maneuvers.

This paper addresses two fundamental challenges in HRV control: (1) Configuration innovation: current composite control systems either prioritize structural simplicity at the cost of maneuverability or achieve multi-axis control through overly complex actuator arrangements [14]. (2) Control robustness: the strong inertial coupling induced by moving masses and the high-frequency disturbances from hypersonic flow dynamics render conventional Model Reference Adaptive Control (MRAC) strategies inadequate [15], particularly in handling unmodeled cross-channel interactions. To address these gaps, we introduce a novel bank-to-turn (BTT) architecture that integrates a single moving mass with differential ailerons, as shown in Figure 1. This configuration achieves three synergistic advantages: (1) Eliminates ablation-vulnerable pitch/yaw surfaces, (2) Utilizes dead space along the central axis. (3) Enables independent thermal management.

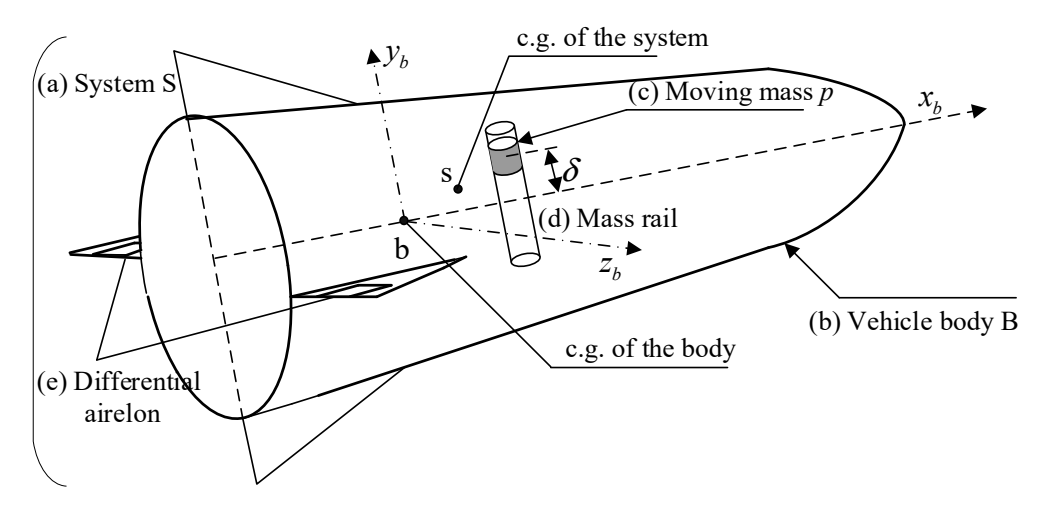


Figure 1. Configuration sketch of the combination BTT control mode with a single moving mass and differential aileron: (a) Entire system S, (b) Vehicle body B, (c) Moving mass, (d) Mass rail, (e) Differential ailerons. Centers of gravity: s (system CG), b (body CG), p (moving mass CG).

To handle the aforementioned complexities and uncertainties that are encountered in flight, adaptive control technology, which has an admirable ability to adjust accord-

Aerospace **2025**, 12, 773 3 of 22

ing to the parameters and uncertainty of the system, has been explored as a possible option for controller design. Early implementations of MRAC demonstrated promise in handling slow-varying uncertainties through online parameter estimation. However, as highlighted by Mohseni et al. [16], MRAC systems exhibit inherent limitations in highfrequency disturbance rejection due to their reliance on persistent excitation conditionscritical shortcoming for hypersonic vehicles subjected to rapid aerodynamic transitions and actuator-induced vibrations. Unlike classical MRAC, L1 architecture decouples estimation and control loops via low-pass filtering [17,18]. This enables the independent compensation of slow parametric drift (e.g., ablation) and fast disturbances (e.g., mass-induced vibrations), and preserves robustness margins via strict gain constraints [19]. Subsequent studies have validated L1 adaptive control's superiority in aerospace applications. For a flexible hypersonic flight vehicle, Khankalantary et al. [20] demonstrated a 40% reduction in tracking error compared to MRAC under thruster failures, attributing this improvement to the L1 method's ability to compensate for actuator saturation. In multi-rotor systems, Wang et al. [21] achieved sub-degree attitude precision despite propeller damage by integrating L1 adaptation with dynamic inversion—a synergy that inspired its adoption in the X-48B aircraft's flight trials [22]. Notably, Banerjee et al. [23] extended these principles to hypersonic gliders, proving that L1-augmented controllers could maintain stability during Mach 8 transitions with $\pm 25\%$ aerodynamic coefficient variations. These advancements collectively underscore L1 control's versatility in handling broad-spectrum uncertainties, yet a critical research void persists in its application to moving mass-actuated systems.

The key theoretical contributions of this paper are as follows: (1) Derivation of a coupled 7-DOF dynamics model that explicitly quantifies inertial coupling effects between the moving mass and rolling motion, providing new insights into cross-channel interaction mechanisms. Established stability criteria for inertial coupling mitigation, proving that roll rates induce catastrophic mode coupling—a critical design boundary for future HRVs. (2) First application of L1 adaptive control to moving mass-aileron composite systems, enabling robust tracking under simultaneous parametric uncertainties, aileron failures, and high-frequency mass-induced disturbances. The remainder of this paper is organized as follows: Section 2 formulates the coupled dynamics model, Section 3 analyzes inertial coupling mechanisms and the effect of rolling motion on the dynamics of moving mas, Section 4 details the L1 adaptive controller design, Section 5 validates performance through comparative simulations, and Section 6 concludes with engineering implications.

2. Formulation of the Dynamical Equations

The internal structure of the maneuverable vehicle controlled by a single moving mass and a differential aileron is shown in Figure 1. The system S, whose center of gravity is denoted by s, is composed of the vehicle body B, whose center of gravity is denoted by b, and the internal moving mass whose center of gravity is denoted by p. The rail of moving mass is parallel to the axis y_b of the body coordinate system $b - x_b y_b z_b$.

The following notation is used in deriving the equations of motion:

- (1) m_B and m_p are the mass of the vehicle body B and the moving mass p, respectively. The mass of system S is $m_S = m_B + m_p$. $\mu = m_p/m_S$ is the mass ratio of the moving mass relative to the system.
- (2) r_s and r_p are the position vectors of the system center of gravity s and the actuator mass p with respect to the inertial reference frame, respectively.
- (3) $\mathbf{r}_{bp} = \begin{bmatrix} l & \delta & 0 \end{bmatrix}^T$ is the position vector of the actuator mass in the body frame. l is the axial coordinate of the moving mass p in the body frame, and the variable δ is the displacement of the moving mass along the rail. $\dot{\delta}$ and $\ddot{\delta}$ are the velocity and

Aerospace 2025, 12, 773 4 of 22

acceleration of the actuator mass along the rail. The position vector of the total system in the body frame is $r_{bs} = \mu r_{bp}$.

- (4) V_B is the inertial velocity vector of the center of mass of the vehicle body B. $\omega = \begin{bmatrix} \omega_x & \omega_y & \omega_z \end{bmatrix}^T$ is the inertial angular velocity vector of the body B, where ω_x , ω_y , and ω_z are the roll, yaw, and pitch rates, respectively, expressed in the body-fixed coordinate system.
- (5) $I_{B/b}$ is the 3 × 3 inertia tensor of the body B about its center of gravity. Where I_x , I_y , I_z are the principal moments of inertia about the body-fixed x-, y-, z-axes, respectively. The inertia tensor is defined in the body-fixed principal axes ($I_{ij} = 0$ for $i \neq j$), eliminating cross-product terms. This alignment is maintained throughout bank manneyers.
- (6) $\frac{{}^Bd(\cdot)}{dt}$ and $\frac{{}^Bd^2(\cdot)}{dt^2}$ are taking the first and second derivatives of the vector with respect to the body-fixed reference frame, respectively. $\frac{{}^Bd(\cdot)}{dt}$ and $\frac{{}^Id^2(\cdot)}{dt^2}$ are taking the first and second derivatives of the vector with respect to the inertial reference frame, respectively.

If a vector is expressed in the frame as $\mathbf{r} = \begin{bmatrix} r_x & r_y & r_z \end{bmatrix}^T$, then the cross-product operator acting on \mathbf{r} expressed in the frame is:

$$\mathbf{r}^{\times} = \begin{bmatrix} 0 & -r_z & r_y \\ r_z & 0 & -r_x \\ -r_x & r_x & 0 \end{bmatrix} \tag{1}$$

The 7-DOF model encompasses:

- Three translational degrees of freedom for the system's center of mass (x, y, z in the inertial frame)
- Three rotational degrees of freedom for vehicle attitude (roll γ , pitch θ , yaw ψ)
- One degree of freedom for moving mass displacement δ along the body-axis rail (Figure 1).

This complete formulation captures both rigid-body dynamics and internal actuation coupling.

2.1. Forces and Moments Model

The hypersonic vehicle can be regarded as a system of particles with constant mass that is only impacted by the force of gravity and aerodynamics. The detailed specifications of the forces and moments exerted on the vehicle are expressed as follows.

(1) F_a is the vector of aerodynamic force acting on the body's center of pressure. M_B is the vector of aerodynamic moments relative to the vehicle body's center of mass. The aerodynamic forces and moments are expressed in the body frame as the following expressions:

$$F_{a} = \begin{bmatrix} -X \\ Y \\ Z \end{bmatrix} = \begin{bmatrix} -C_{x} \\ C_{y}^{\alpha} \alpha \\ C_{z}^{\beta} \beta \end{bmatrix} qS_{B}$$
 (2)

$$\mathbf{M}_{B} = \begin{bmatrix} M_{Bx} \\ M_{By} \\ M_{Bz} \end{bmatrix} = \begin{bmatrix} m_{x}^{\delta_{a}} \delta_{a} + \frac{m_{x}^{\omega_{x}} L}{v} \omega_{x} \\ m_{y}^{\beta} \beta + \frac{m_{y}^{\omega_{y}} L}{v} \omega_{y} \\ m_{z}^{\alpha} \alpha + \frac{m_{z}^{\omega_{z}} L}{v} \omega_{z} \end{bmatrix} qS_{B}L$$
 (3)

where α and β are the angle of attack (AOA) and sideslip angle, respectively. Consistent with hypersonic reentry vehicle literature [9,13], we employ missile-axis aerodynamic coefficients: C_x is the drag coefficient, and C_y^{α} and C_z^{β} are the partial derivatives of the normal forces coefficients with respect to the angle of attack and sideslip angle, respectively.

Aerospace **2025**, 12, 773 5 of 22

 m_z^α and m_y^β are the partial derivatives of the pitching moment and the yawing moment coefficients with respect to the angle of attack and sideslip angle, respectively. $m_x^{\omega_x}$, $m_y^{\omega_y}$ and $m_z^{\omega_z}$ are the aerodynamic damping coefficients, respectively. $q = \rho |V_B|^2/2$ is the dynamic pressure, ρ is the atmospheric density, S_B is the cross-sectional area, L is the reference length. δ_a is the deflection angle of the aileron, and $m_x^{\delta_a}$ is the control coefficient of the differential aileron.

The aerodynamic reference area S_B (0.5 m²) corresponds to the vehicle's planform area. The nominal flight condition (Mach 10 at 15 km altitude) yields a dynamic pressure of: $q = \rho |V_B|^2/2 = 814,000$ Pa. This high dynamic pressure (approximately 17,000 lbf/ft²) corresponds to an equivalent airspeed (EAS) of approximately 1041 m/s (2024 knots) and a calibrated airspeed (CAS) of approximately 1037 m/s (2018 knots). Such extreme dynamic pressure conditions are characteristic of the lower hypersonic flight corridor and result in significant aerodynamic loads. The control surfaces must overcome these high loads, which pose a challenge for the control authority, especially when combined with the high inertial coupling effects.

- (2) G_S is the gravity vector of the system. $M_{ab} = [M_{fx} \quad 0 \quad 0]^T$ is the disturbance roll moment caused by the asymmetric ablation of the vehicle.
- (3) N is the force exerted by the vehicle body on the actuator mass, whose body-axis components are $N = \begin{bmatrix} N_x & F_u & N_z \end{bmatrix}^T$. Where N_x and N_z are the forces in the direction of the body-axis x_b and z_b exerted by the vehicle body on the actuator mass, and F_u is the driving force generated by the servo motor on the actuator mass.

2.2. System Dynamical Equation

According to the momentum theorem, the system's translational dynamics are given by Equation (4)

$$m_S \frac{{}^{I}d^2 \mathbf{r}_s}{dt^2} = \sum \mathbf{F}_s \Rightarrow m_S \left(\frac{{}^{B}d\mathbf{V}_B}{dt} + \boldsymbol{\omega} \times \mathbf{V}_B + \mu \frac{{}^{I}d^2 \mathbf{r}_{bp}}{dt^2} \right) = \mathbf{F}_a + m_S \mathbf{g}$$
(4)

The motions of the actuator mass are described by Equation (5):

$$m_p \frac{{}^{I}d^2 \mathbf{r}_p}{dt^2} = \sum \mathbf{F}_p \Rightarrow m_p \left(\frac{{}^{B}d\mathbf{V}_B}{dt} + \boldsymbol{\omega} \times \mathbf{V}_B + \frac{{}^{I}d^2 \mathbf{r}_{bp}}{dt^2} \right) = \mathbf{N} + m_p \mathbf{g}$$
 (5)

According to the angular momentum theorem, the system's rotational dynamics are given by Equation (6):

$$\frac{{}^{I}d\mathbf{H}_{S}}{dt} = \sum \mathbf{M}_{S} \Rightarrow \mathbf{I}_{B/b} \frac{{}^{B}d\boldsymbol{\omega}}{dt} + (1-\mu)\mathbf{r}_{bp} \times m_{p} \frac{{}^{I}d^{2}\mathbf{r}_{bp}}{dt^{2}} + \boldsymbol{\omega} \times (\mathbf{I}_{B/B^{*}} \cdot \boldsymbol{\omega}) = \mathbf{M}_{B} + \mathbf{M}_{ab} - \mu \mathbf{r}_{bp} \times \mathbf{F}_{a}$$
(6)

where H_S represents the total angular momentum of the system with respect to the mass center of the system, and $\sum M_S$ is the total external moments acting on the flight vehicle. Expanding Equations (4)–(6) with respect to the body frame, the vehicle's translational and rotational dynamics equations, and the moving mass's translational dynamic equation deduced in the body coordinate system are given by Equations (7)–(9):

$$m_S \dot{V}_B = G_S + F_a - m_S \omega \times V_B - m_p (\ddot{r}_{bp} + 2\omega \times \dot{r}_{bp} + \dot{\omega} \times r_{bp} \omega \times (\omega \times r_{bp}))$$
 (7)

$$\mathbf{I}_{B/b}\dot{\boldsymbol{\omega}} = \mathbf{M}_B - \mathbf{r}_{bs} \times \mathbf{F}_a + \mathbf{M}_{ab} - \boldsymbol{\omega} \times (\mathbf{I}_{B/b}\boldsymbol{\omega}) - (\mathbf{r}_{bp} - \mathbf{r}_{bs}) \times m_p \left(\ddot{\mathbf{r}}_{bp} + 2\boldsymbol{\omega} \times \dot{\mathbf{r}}_{bp} + \dot{\boldsymbol{\omega}} \times \mathbf{r}_{bp} + \boldsymbol{\omega} \times (\boldsymbol{\omega} \times \mathbf{r}_{bp}) \right)$$
(8)

$$\ddot{\delta} = \boldsymbol{b}_{1}^{T} \left[\frac{\boldsymbol{G}_{S}}{m_{S}} - \dot{\boldsymbol{V}}_{B} - \boldsymbol{\omega} \times \boldsymbol{V}_{B} - 2\boldsymbol{\omega} \times \dot{\boldsymbol{r}}_{bp} - \dot{\boldsymbol{\omega}} \times \boldsymbol{r}_{bp} \right. \left. - \boldsymbol{\omega} \times (\boldsymbol{\omega} \times \boldsymbol{r}_{bp}) \right] + \frac{1}{m_{p}} F_{u}$$
(9)

Aerospace **2025**, 12, 773 6 of 22

where $\boldsymbol{b}_{1}^{T} = \begin{bmatrix} 0 & 1 & 0 \end{bmatrix}$ is a basis unit vector, $\dot{\boldsymbol{V}}_{B}$, $\dot{\boldsymbol{\omega}}$, $\dot{\boldsymbol{r}}_{bp}$, $\ddot{\boldsymbol{r}}_{bp}$ are taking the first or second derivative of the vectors with respect to time in the body-fixed reference frame, respectively.

3. Dynamic Characteristics Analysis of Composite Control Hypersonic Vehicle

3.1. Inertial Coupling Mechanism

Instability induced by multiple coupling phenomena constitutes a principal challenge in bank-to-turn (BTT) control systems. Among these, inertial coupling arising from rolling maneuvers represents a critical destabilizing mechanism. Inertial coupling refers to adverse moments generated by the vehicle's rotation about non-principal inertia axes. Excessive roll angular velocity ω_x and the pitch and yaw channels will be greatly affected by the inertial moments in the case that roll angular velocity ω_x amplifies inertial moments, which detrimentally affect pitch and yaw channels. Notably, such inertial effects may dominate static stabilizing moments, therefore compromising attitude stabilization. The classical roll coupling parameter $(I_x - I_y)/I_z = -0.5$ indicates strong pitch-yaw cross-coupling during rolling, consistent with Philips (1948) [24].

To analytically investigate this phenomenon, we consider a simplified scenario where the vehicle undergoes constant roll angular velocity ω_x^* about its lateral axis while maintaining constant flight velocity. Applying small-perturbation linearization and neglecting higher-order rolling dynamics, the linearized equations governing fast roll perturbation motion are derived as:

$$\Delta \dot{\alpha} \simeq \Delta \omega_{z} - \omega_{x}^{*} \Delta \beta
\Delta \dot{\beta} \simeq \Delta \omega_{y} + \omega_{x}^{*} \Delta \alpha
\Delta \dot{\omega}_{z} = -A \Delta \omega_{y} \omega_{x}^{*} + \overline{M}_{\alpha} \Delta \alpha + \overline{M}_{d} \omega_{z} + \overline{M}_{\delta} \Delta \delta
\Delta \dot{\omega}_{y} = B \Delta \omega_{z} \omega_{x}^{*} + \overline{N}_{\beta} \Delta \beta + \overline{N}_{d} \omega_{y}$$
(10)

where the coefficients are defined by:

$$A = \frac{I_{y} - I_{x} - m_{p}(1 - \mu)\delta^{2}}{I_{z} + m_{p}(1 - \mu)\delta^{2}}, \quad B = \frac{I_{z} - I_{x}}{I_{y}}$$

$$\overline{M}_{\alpha} = \frac{qS_{B}Lm_{z}^{\alpha}}{I_{z} + m_{p}(1 - \mu)\delta^{2}}, \quad \overline{N}_{\beta} = \frac{qS_{B}Lm_{y}^{\beta}}{I_{y}}$$

$$\overline{M}_{d} = \frac{\left(qS_{B}L^{2}\frac{m_{z}^{\omega^{2}}}{2v} - 2m_{p}(1 - \mu)\delta\dot{\delta}\right)}{\left(I_{z} + m_{p}(1 - \mu)\delta^{2}\right)}$$

$$\overline{N}_{d} = qS_{B}L^{2}\frac{m_{y}^{\omega}}{2vI_{y}}, \quad \overline{M}_{\delta} = \frac{-\mu C_{x}qS_{B}}{I_{z} + m_{p}(1 - \mu)\delta^{2}}$$
(11)

The characteristic equation corresponding to Equation (10) is expressed as:

$$\lambda^4 + a_1 \lambda^3 + a_2 \lambda^2 + a_3 \lambda + a_4 = 0 \tag{12}$$

Coefficients in Equation (12) depend on the vehicle's inertia tensor, aerodynamic parameters, moving mass position, and rolling motion characteristics. By neglecting damping terms (\overline{M}_d and \overline{N}_d), Equation (12) are simplified as:

$$\lambda^4 + a_2 \lambda^2 + a_4 = 0 \tag{13}$$

Stability criteria for fast roll dynamics, derived from Equation (13), necessitate $a_2 > 0$ and $a_4 > 0$. Vehicles exhibiting directional and longitudinal static stability inherently satisfy $a_2 > 0$ can be guaranteed. Consequently, the critical condition for steady rolling reduces to:

$$a_4 = \left(A\omega_x^{*2} + \overline{M}_\alpha\right) \left(B\omega_x^{*2} + \overline{N}_\beta\right) > 0 \tag{14}$$

Aerospace 2025, 12, 773 7 of 22

Defining stability bounds ω_1 and ω_2 as follows:

$$\omega_{1} = \sqrt{-\overline{M}_{\alpha}/A} = \sqrt{-\overline{M}_{\alpha} \frac{I_{z} + m_{p}(1-\mu)\delta^{2}}{I_{y} - I_{x} - m_{p}(1-\mu)\delta^{2}}},$$

$$\omega_{2} = \sqrt{-\overline{N}_{\beta}/B} = \sqrt{-\overline{N}_{\beta} \frac{I_{y}}{I_{z} - I_{x}}}$$
(15)

Equation (14) resolves into two equivalent constraints:

$$|\omega_{\mathfrak{r}}^*| > \omega_1 \text{ and } |\omega_{\mathfrak{r}}^*| > \omega_2$$
 (16)

or
$$|\omega_x^*| < \omega_1 \text{ and } |\omega_x^*| < \omega_2$$
 (17)

For vehicles with dual-axis static stability, adherence to Equation (16) ensures rotation about principal inertia axes. Angle of attack and sideslip angle will transform into each other periodically, and the rapid transformation will precipitate performance degradation or instability. While Equation (17) guarantees alignment with the velocity vector, thereby mitigating motion coupling. The permissible roll rate is thus bounded by the lesser of ω_1 and ω_2 , establishing a conservative operational threshold.

3.2. Actuator Mass-Roll Dynamics Interaction

The translational dynamics equation of moving mass, governed by Equation (9), exhibits coupling with the differential terms \dot{V}_B and $\dot{\omega}$. To systematically analyze the actuator mass dynamics, a decoupled formulation is derived as follows.

Initially, substituting V_B from Equation (7) into Equation (9) yields:

$$\ddot{\delta} = \left(\omega_x^2 + \omega_z^2\right)\delta - \omega_x \omega_y l + \frac{1}{m_p(1-\mu)}F_u - \frac{1}{m_S(1-\mu)}Y - l\dot{\omega}_z \tag{18}$$

The influence of roll angular velocity on the actuator mass dynamics in two primary mechanisms: (1) Explicit Appearance: The roll angular velocity directly appears in the actuator mass's dynamic equation; (2) Implicit coupling: Cross-channel interactions between roll and pitch attitudes, which modulate pitch angular acceleration. Conventional skid-to-turn (STT) control architectures often neglect the $\dot{\omega}_z$ -dependent term in Equation (18).

As illustrated by open-loop simulations under constant servo force F_u , Figure 2a demonstrates the nominal displacement response, while Figure 2b quantifies the displacement error under varying initial roll rates ω_x when the initial angle of attack $\alpha_0=0^\circ$ and sideslip angle $\beta_0=0^\circ$. From the figure, when $\omega_x=0 \, \mathrm{rad/s}$, the effect of ω_x on the actuator mass's motion is minimal. Compared to the actuator mass displacement of tens of centimeters, the tracking error is two to three orders of magnitude smaller. However, as the roll angular velocity increases, the impact of ω_x , becomes increasingly significant. For example, at $\omega_x=6\pi \, \mathrm{rad/s}$ the error escalates to 0.04 m, highlighting the criticality of roll coupling in bank-to-turn (BTT) control design. Consequently, the ω_x -dependent term cannot be omitted in BTT systems, necessitating further decoupling analysis.

The Equation (18) only contains the differential term $\dot{\omega}_z$. Then the expression of $\dot{\omega}_z$ will be given as follows. According to the attitude dynamic Equation (8), there is a differential term which contains $\dot{\omega}$ in the right of the equation. Define a new inertia tensor matrix I as follows:

$$I = I_{B/b} + m_p (\mathbf{r}_{bp}^{\times} - \mathbf{r}_{bs}^{\times}) (\mathbf{r}_{bp}^{\times})^{\mathrm{T}} = I_{B/b} + \Delta I$$
(19)

Aerospace **2025**, 12, 773 8 of 22

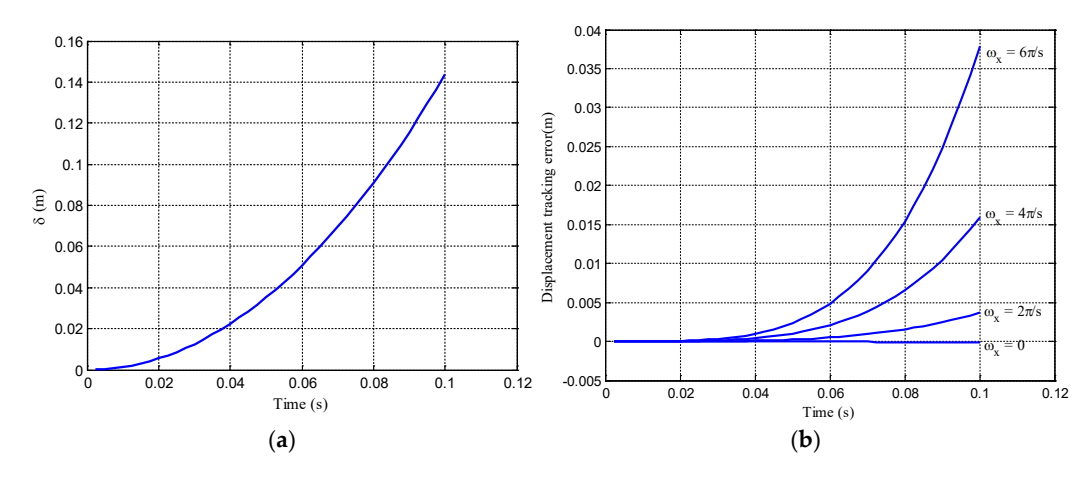


Figure 2. Influence of different initial roll angular velocities on displacement of the moving mass under constant servo force ($F_u = 500 \text{ N}$). Total system mass $m_S = 1000 \text{ kg}$, moving mass $m_p = 100 \text{ kg}$ ($\mu = 0.1$). (a) Displacement of moving mass, (b) Displacement tracking error vs. roll angular velocity.

Then the attitude dynamic Equation (8) can be transformed into:

$$\dot{\boldsymbol{\omega}} = \boldsymbol{I}^{-1}\boldsymbol{M} = (\boldsymbol{I}_{B/b} + \Delta \boldsymbol{I})^{-1} \begin{bmatrix} M_x \\ M_y \\ M_z \end{bmatrix}$$
 (20)

where ΔI represents the additional moment of inertia generated by the motion of the moving mass. The expressions of ΔI and the component of moment M are described by Equations (21) and (22).

$$\Delta \mathbf{I} = m_p (1 - \mu) \begin{bmatrix} \delta^2 & -\delta l & 0 \\ -\delta l & l^2 & 0 \\ 0 & 0 & \delta^2 + l^2 \end{bmatrix} = \begin{bmatrix} \Delta I_x & \Delta I_{xy} & 0 \\ \Delta I_{xy} & \Delta I_y & 0 \\ 0 & 0 & \Delta I_z \end{bmatrix}$$
(21)

$$M_{x} = M_{Bx} + M_{\delta_{a}} + M_{fx} - (I_{z} - I_{y})\omega_{y}\omega_{z} - 2m_{p}(1 - \mu)\delta\dot{\delta}\omega_{x} - \mu\delta Z - m_{p}\delta(1 - \mu)\omega_{z}(l\omega_{x} + \delta\omega_{y})$$

$$M_{y} = M_{By} - (I_{x} - I_{z})\omega_{x}\omega_{z} + \mu_{p}lZ + m_{p}(1 - \mu)\left[l^{2}\omega_{x}\omega_{z} + l\delta\omega_{y}\omega_{z} + 2l\delta\omega_{x}\right]$$

$$M_{z} = M_{Bz} - (I_{y} - I_{x})\omega_{x}\omega_{y} - \mu lY - \mu\delta X - m_{p}(1 - \mu)\left(\ddot{\delta}l + l^{2}\omega_{x}\omega_{y}\right)$$

$$+ m_{p}(1 - \mu)\delta(-2\dot{\delta}\omega_{z} + \delta\omega_{y}\omega_{x} - l\omega_{y}^{2} + l\omega_{x}^{2})$$
(22)

So the expression of $\dot{\omega}_z$ can be given by substituting Equation (18) into M_z in Equation (22):

$$\dot{\omega}_{z} = (I_{z} + \Delta I_{z})^{-1} M_{z}$$

$$= (I_{z} + m_{p}(1 - \mu)\delta^{2})^{-1} \left[M_{Bz} - (I_{y} - I_{x})\omega_{x}\omega_{y} - \mu\delta X - m_{p}(1 - \mu)\delta l \left(\omega_{y}^{2} + \omega_{z}^{2}\right) + m_{p}(1 - \mu)\delta \left(-2\dot{\delta}\omega_{z} + \delta\omega_{y}\omega_{x}\right) - lF_{u} \right]$$
(23)

By substituting Equation (23) into Equation (18), the decoupling dynamic equation of the actuator mass is given:

$$\ddot{\delta} = (\omega_x^2 + \omega_z^2)\delta - \omega_x \omega_y l - \frac{k_1}{m_p l} M_{Bz} - \frac{k_1}{m_p l} M_{Rz} + \frac{k_1}{m_p l} (I_y - I_x) \omega_x \omega_y + \frac{1}{m_p} (k_2 X - k_3 Y) + k_4 \frac{F_u}{m_p} + k_5 (\omega_y^2 + \omega_z^2) \delta - k_6 \omega_y \omega_x \delta + k_7 \omega_z \delta$$
(24)

where the expression of parameters k_i , (i = 1, 2, ... 7) are provided as follows.

$$k_{1} = \frac{m_{p}l^{2}}{I_{z} + m_{p}(1-\mu)\delta^{2}}, \quad k_{2} = \frac{\mu m_{p}l\delta}{I_{z} + m_{p}(1-\mu)\delta^{2}}, \quad k_{3} = \frac{\mu}{1-\mu}$$

$$k_{4} = k_{1} + \frac{1}{1-\mu}, \quad k_{5} = (1-\mu)k_{1}, \quad k_{6} = \frac{(1-\mu)m_{p}l\delta}{I_{z} + m_{p}(1-\mu)\delta^{2}}, \quad k_{7} = 2k_{6}$$
(25)

Equation (24) rigorously describes the actuator mass dynamics as a function of angular velocity $(\omega_x, \omega_y, \omega_z)$ and nd moving mass states , δ , $\dot{\delta}$,, providing a foundation for robust controller synthesis.

- 3.3. Roll Control Challenges Compared with STT and Spin Control Mode
 - The roll control objectives vary significantly across different actuation architectures:
- (1) Spin-Stabilized Systems: For vehicles employing a single actuator mass, roll control aims to regulate angular velocity ω_x within a frequency range synchronized with the mass's motion period—typically $1\times$ or $2\times$ the actuator frequency. This synchronization ensures that the moving mass-induced center of gravity (CoG) shift generates predictable lateral moments for attitude adjustment.
- (2) STT Systems: Dual-actuator configurations prioritize roll angle γ stabilization, maintaining $\gamma \approx 0$ through counteracting mass displacements.
- (3) BTT Systems: Uniquely, BTT architectures demand dual functionality—stabilizing the roll channel while tracking dynamic roll commands. This imposes stringent requirements on tracking precision, transient response, and robustness to inertial coupling.

According to Equation (8), the displacement and velocity of the actuator mass have a great influence on the roll channel. Figure 3 shows the influence of the static or moving actuator mass on the roll channel. The full line represents the roll angle responding to the static actuator mass. The dash line represents the roll angle responding to high-frequency sinusoidal movement whose cycle is 0.1 s for the actuator mass. As indicated in Figure 4, in order to make the reentry vehicle maneuver fast, the high-frequency movement of the actuator mass will have a greater high-frequency disturbance on the roll channel. The MRAC method has some limit conditions on the frequency of parameters and disturbance. The convergence rate, transient error, and tracking error will be affected greatly when the system is affected by the external disturbance signals with a high frequency.

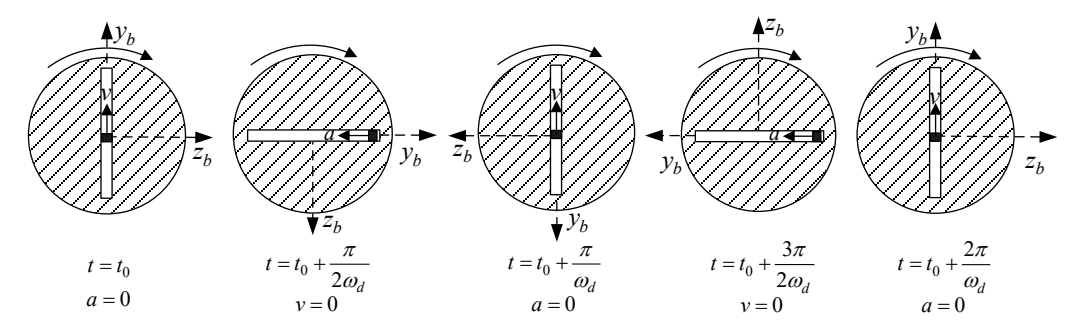


Figure 3. The movement cycle of the moving mass is equal to the rotation cycle of the spin vehicle.

To address these challenges, the next section introduces an L1 adaptive roll controller, specifically designed to attenuate mass-induced disturbances while preserving BTT tracking performance.

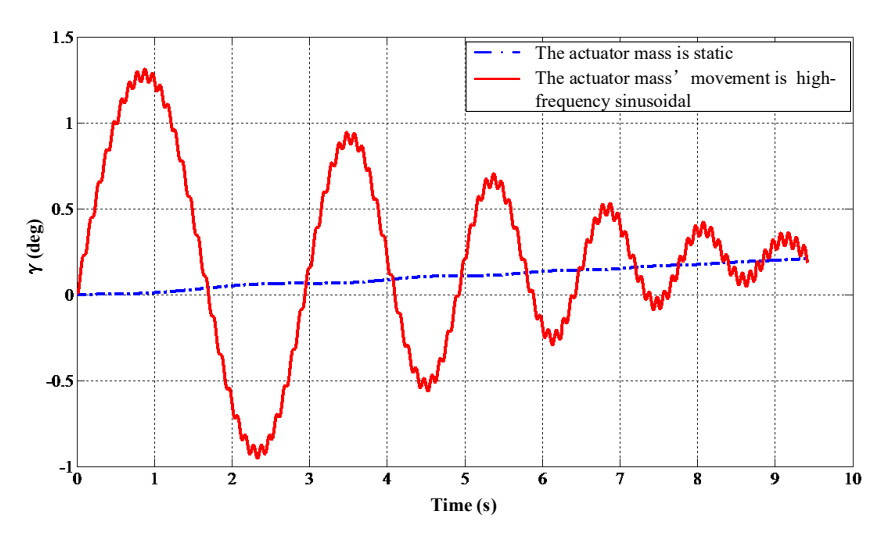


Figure 4. Influence on the roll channel from the high-frequency movement of the actuator mass (10 Hz oscillation $\delta = \pm 0.1$ m).

4. Controller Design

This section presents the design of a BTT control law for a hypersonic vehicle employing composite actuation via a moving mass and differential ailerons. Under the standard BTT assumption of yaw-channel stability, pitch and roll dynamics are governed by the following simplified equations:

$$(I_x + \Delta I_x)\dot{\omega}_x + \Delta I_{xy}\dot{\omega}_y = \left(\frac{qS_BL^2m_x^{\omega_x}}{v} - 2m_p(1-\mu)\delta\dot{\delta}\right)\omega_x + qS_BLm_x^{\delta_a}\delta_a + M_{fx} + \widetilde{I}_{yz}\omega_y\omega_z - \mu qS_BC_z^{\beta}\delta\beta - m_p(1-\mu)l\delta\omega_x\omega_z$$
(26)

$$(I_z + \Delta I_z)\dot{\omega}_z = \left(\frac{qS_B m_z^{\omega_z} L^2}{v} - 2m_p (1 - \mu)\delta\dot{\delta}\right)\omega_z + \widetilde{I}_{xy}\omega_x\omega_y + qS_B\left(m_z^{\alpha}L - \mu lC_y^{\alpha}\right)\alpha - \mu qS_BC_x\delta$$

$$-m_p (1 - \mu)l\ddot{\delta} + m_p (1 - \mu)\delta l(\omega_x^2 - \omega_y^2)$$
(27)

where ΔI_x , ΔI_{xy} , ΔI_z denote the additional moments of inertia generated by the motion of the actuator mass, with ΔI_{xy} mediating cross-channel coupling between lateral and directional axes. The mathematical expressions governing these inertial perturbations are subsequently derived as follows.

$$\widetilde{I}_{xy} = I_x - I_y + m_p (1 - \mu) (\delta^2 - l^2)$$

$$\widetilde{I}_{yz} = I_y - I_z - m_p (1 - \mu) \delta^2$$

$$\Delta I_x = m_p (1 - \mu) \delta^2$$

$$\Delta I_{xy} = -m_p (1 - \mu) \delta l$$

$$\Delta I_z = m_p (1 - \mu) (\delta^2 + l^2)$$

The nonlinear dynamic system can be formulated in an affine state–space representation as:

$$\dot{x}_1 = f_1(x_1) + g_1(x_1)x_2
\dot{x}_2 = f_2(x_1, x_2) + g_2(x_1, x_2)u
y = x_1$$
(28)

where $\mathbf{x}_1 = \begin{bmatrix} \gamma & \alpha \end{bmatrix}^T$, $\mathbf{x}_2 = \begin{bmatrix} \omega_x & \omega_z \end{bmatrix}^T$ represents the state vector. The variable γ represents the actual roll angle. $\mathbf{u} = \begin{bmatrix} \delta_a & \delta \end{bmatrix}^T$ denotes the control input vector. \mathbf{y} corresponds to the system output vector.

$$f_1(\mathbf{x}_1) = \begin{bmatrix} 0 \\ -\frac{C_y^{\alpha}qS}{m_sV}\alpha \end{bmatrix}, \quad \mathbf{g}_1(\mathbf{x}_1) = \begin{bmatrix} 1 & \cos\gamma\tan\psi \\ 0 & 1 \end{bmatrix}$$

$$f_2(\mathbf{x}_1,\mathbf{x}_2) = \begin{bmatrix} (I_x + \Delta I_x)^{-1} \left(\frac{qS_BL^2m_x^{\omega x}}{v} - 2m_p(1-\mu)\delta\dot{\delta}\right)\omega_x + M_{fx} + \tilde{I}_{yz}\omega_y\omega_z - \mu qS_BC_z^{\beta}\delta\beta \\ -m_p(1-\mu)l\delta\omega_x\omega_z - \Delta I_{xy}\dot{\omega}y \end{bmatrix}$$

$$(I_z + \Delta I_z)^{-1} \left(\frac{qS_Bm_z^{\omega z}L^2}{v} - 2m_p(1-\mu)\delta\dot{\delta}\right)\omega_z + \tilde{I}_{xy}\omega_x\omega_y + qS_B\left(m_z^{\alpha}L - \mu lC_y^{\alpha}\right)\alpha \\ -m_p(1-\mu)l\ddot{\delta} + m_p(1-\mu)\delta l(\omega_x^2 - \omega_y^2) \end{bmatrix}$$

$$\mathbf{g}_2(\mathbf{x}_1,\mathbf{x}_2) = \begin{bmatrix} \frac{m_x^{\delta a}qS_BL}{I_x + \Delta I_x} & 0 \\ 0 & -\frac{\mu C_xqS_B}{I_z + \Delta I_z} \end{bmatrix}$$

To comprehensively address modeling imperfections, the proposed control architecture explicitly incorporates parametric uncertainties, input uncertainties, and functional uncertainties encompassing external disturbances and unmodeled dynamics. Consequently, the governing Equation (28) can be reformulated in compact notation as:

$$\dot{x}_1 = g_1(\Lambda_1 x_2 + v_1) + f_1 \tag{29}$$

$$\dot{x}_2 = g_2(\Lambda_2 u + v_2) + f_2 \tag{30}$$

The parameter uncertainty, input uncertainty, and function uncertainty (such as the external disturbances and modeling errors) are described by the control effectiveness Λ_1 , Λ_2 and the nonlinear terms v_1 , v_2 . We synthesize an adaptive controller that guarantees bounded-error tracking of AOA and roll angle references under time-varying disturbances, achieved through synergistic integration of dynamic inversion and L1 adaptive control methodologies. Figure 5 illustrates the hierarchical architecture of the proposed control system, with subsequent subsections providing detailed component analyses.

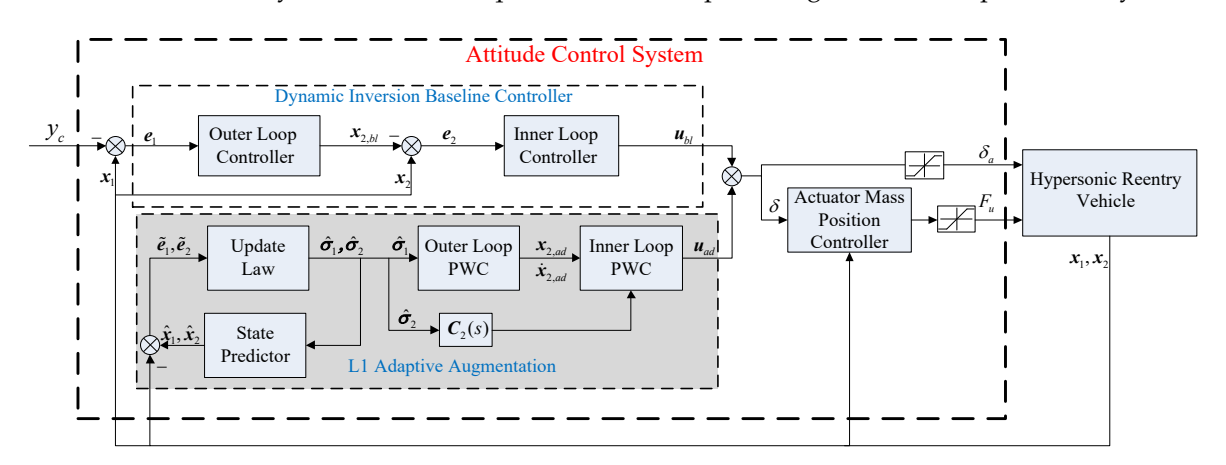


Figure 5. Architectural diagram of the adaptive attitude control system.

4.1. Baseline Dynamic Inversion Controller

Following the timescale separation principle [25], the system dynamics are decomposed into two distinct operational regimes: fast-timescale inner-loop rotational dynamics and slow-timescale outer-loop attitude dynamics. For outer-loop controller synthesis, the pseudo-control command $x_{2,bl}$ is designed such that asymptotic convergence of body angular rates x_2 to reference trajectories $x_{2,bl}$ ensures tracking of guidance-generated command signals y_c . Correspondingly, the inner-loop baseline control law u_{bl} guarantees x_2 tracks the pseudo-control $x_{2,bl}$.

Defining the outer-loop and inner-loop tracking errors as $e_1 = y - y_c = x_1 - y_c$ and $e_2 = x_2 - x_{2,bl}$, respectively, the baseline dynamic inversion control laws are formulated as:

$$x_{2,bl} = g_1^{-1} \left(-f_1 - k_{P1}e_1 + \dot{y}_c \right) \tag{31}$$

$$u_{bl} = g_2^{-1} \left(-f_2 - k_{P2} e_2 + \dot{x}_{2,bl} \right) \tag{32}$$

where k_{P1} and k_{P2} represent positive-definite diagonal gain matrices. The outer-loop compensator (31) and the inner-loop regulator (32) include a proportional error feedback of the attitude angle and the body angular rate, respectively. A classical second-order integral filter [26] is used in this paper in order to eliminate the analytic computation of \dot{y}_c and $\dot{x}_{2,bl}$, which will be used as a reference in the dynamic inversion procedure.

4.2. L1 Adaptive Augmentation

To address coupled dynamic uncertainties inherent in hypersonic systems, the baseline control law is augmented with an L_1 adaptive control law. L_1 adaptive state feedback controller derives real-time estimates of composite disturbances through bandwidthlimited compensation via low-pass filters, as illustrated in the enhanced system architecture (Figure 5). An L_1 adaptive augmentation was implemented with three core innovations:

(1) Dual-Decoupled State Predictors:

The attitude dynamics from Equations (29) and (30) are reformulated to facilitate adaptive element synthesis:

$$\dot{x}_1 = g_1 x_2 + f_1 + \sigma_1 \tag{33}$$

$$\dot{x}_2 = g_2 u + f_2 + \sigma_2 \tag{34}$$

where σ_1 and σ_2 represent lumped uncertainty vectors encompassing outer-loop and inner-loop perturbations, respectively. The uncertainties σ_1 and σ_2 , which can be estimated by L₁ adaptive controller, summarize the control effectiveness Λ_1 , Λ_2 and the nonlinear uncertainties v_1 , v_2 as follows.

$$\sigma_1 = g_1[(\Lambda_1 - I)x_2 + v_1]
\sigma_2 = g_2[(\Lambda_2 - I)u + v_2]$$
(35)

A dual-state predictor structure for outer-loop (attitude) and inner-loop (angular rate) dynamics is implemented for uncertainty estimation:

$$\dot{\hat{x}}_1 = g_1 x_2 + f_1 + \hat{\sigma}_1 - k'_{P1} \tilde{e}_1 \tag{36}$$

$$\dot{\hat{x}}_2 = g_2 u + f_2 + \hat{\sigma}_2 - k'_{P2} \tilde{e}_2 \tag{37}$$

where \hat{x}_1 and \hat{x}_2 denote predicted state derivatives, with prediction errors defined as $\tilde{e}_1 = \hat{x}_1 - x_1$ and $\tilde{e}_2 = \hat{x}_2 - x_2$. Error dynamics are governed by:

$$\dot{\tilde{e}}_1 = -k'_{P1}\tilde{e}_1 + \hat{\sigma}_1 - \sigma_1 \tag{38}$$

$$\dot{\tilde{e}}_2 = -k'_{P2}\tilde{e}_2 + \hat{\sigma}_2 - \sigma_2 \tag{39}$$

where k'_{P1} and k'_{P2} represent positive-definite stabilization gain matrices.

(2) Piecewise-Constant Update Law:

Following a similar argument as in Section 3.3 of [27], the PWC (Piecewise Constant) update law for the uncertainty estimate $\hat{\sigma}_1$ and $\hat{\sigma}_2$ are given by

$$\hat{\sigma}_{1}(t) = -\mathbf{\Phi}_{1}^{-1} \mu_{1}(iT_{s}), \qquad t \in [iT_{s}, (i+1)T_{s}]
\mathbf{\Phi}_{1} = (-k'_{P1})^{-1} (e^{-k'_{P1}T_{s}} - \mathbf{I})
\mu_{1}(iT_{s}) = e^{-k'_{P1}T_{s}} \tilde{e}_{1}$$
(40)

$$\hat{\sigma}_{2}(t) = -\mathbf{\Phi}_{2}^{-1} \mu_{2}(iT_{s}), \qquad t \in [iT_{s}, (i+1)T_{s}]
\mathbf{\Phi}_{2} = (-\mathbf{k'}_{P2})^{-1} (e^{-\mathbf{k'}_{P2}T_{s}} - \mathbf{I})
\mu_{2}(iT_{s}) = e^{-\mathbf{k'}_{P2}T_{s}} \widetilde{e}_{2}$$
(41)

where i = 0, 1, 2, ... and T_s denotes the adaptation update rate constrained by hardware sampling limitations [27]. The uncertainties can be estimated by the analytical Equations (40) and (41). The design parameters only include the feedback gains and the adaptation update rate. In this paper, the update rate is chosen as $T_s = 10$ ms. The gains are chosen by designing the prediction error dynamics according to the error dynamics of the baseline controller.

Based on the uncertainty estimates described above, the control law of the adaptive augmentation is derived. For the outer dynamics, an adaptive body angular rate control law $x_{2,ad}$ is derived to augment the baseline control $x_{2,bl}$, in order to compensate for the outer uncertainties Λ_1 and v_1 . For the inner dynamics, an adaptive pseudo-control law u_{ad} is designed to ensure that x_2 tracks the body angular rate command x_{2c} despite the inner uncertainties Λ_2 and v_2 . So the body angular rate command v_2 is given as follows.

$$x_{2c} = x_{2.bl} + x_{2.ad} (42)$$

Substituting the control law Equations (31) and (42) into the outer-loop dynamics Equation (33), the closed-loop outer error dynamics is given by:

$$\dot{e}_1 = -k_{P1}e_1 - k_{I1}e_{I1} + g_1x_{2,ad} + \sigma_1 \tag{43}$$

(3) Bandwidth-Limited Adaptation:

According to the Reference [27] and Equation (43), the body angular rate adaptive control is given by

$$\mathbf{x}_{2,ad} = -C_1(s)\mathbf{g}_1^{-1}\hat{\sigma}_1 \tag{44}$$

where $C_1(s)$ is a diagonal low-pass transfer function matrix. Then, for the inner dynamics, the augmented pseudo-control u_c are defined as

$$u_c = u_{bl} + u_{ad} \tag{45}$$

Substituting the control law Equations (32) and (45) into the inner-loop dynamics Equation (34)

$$\dot{x}_2 = -k_{P2}e_2 + \dot{x}_{2,bl} + g_2u_{ad} + \sigma_2 \tag{46}$$

In order to ensure that x_2 tracks the augmented body angular rate command x_{2c} , the L1 control law u_{ad} is formulated as

$$\mathbf{u}_{ad} = -C_2(s)\mathbf{g}_2^{-1}\hat{\sigma}_2 + \mathbf{g}_2^{-1}(\mathbf{k}_{P2}\mathbf{x}_{2,ad} + \dot{\mathbf{x}}_{2,ad})$$
(47)

where $C_2(s)$ is a diagonal low-pass transfer function matrix. Low-pass filters confine adaptive action to critical frequencies, and this prevents high-frequency noise amplification while compensating for mass-induced disturbances. The first term in Equation (47) com-

Aerospace 2025, 12, 773 14 of 22

pensates for the inner uncertainties σ_2 , while the latter two terms account for the adaptive contribution for the outer loop. The designs of the filters $C_1(s)$ and $C_2(s)$ used in the control laws Equations (44) and (47) are driven by bandwidth investigations of the considered vehicle dynamics.

4.3. Actuator Mass Position Controller

Conventional approaches often neglect inertial coupling effects in actuator dynamics through angular acceleration term omission. This study develops a feedback linearization and sliding-mode control strategy for precision tracking of mass displacement commands δ_c generated by the attitude controller. In this paper, the actuator mass position controller is designed based on sliding-mode control theory. The translational dynamics from Equation (24) are expressed in state–space form:

$$\ddot{\delta} = f_{\delta}(\mathbf{x}_{1}, \mathbf{x}_{2}, \delta, \dot{\delta}) + g_{\delta}F_{u} \tag{48}$$

where

$$f_{\delta}\left(\mathbf{x}_{1}, \mathbf{x}_{2}, \delta, \dot{\delta}\right) = \left(\omega_{x}^{2} + \omega_{z}^{2}\right)\delta - \omega_{x}\omega_{y}l - \frac{k_{1}}{m_{p}l}M_{Bz} - \frac{k_{1}}{m_{p}l}M_{Rz} + \frac{k_{1}}{m_{p}l}\left(I_{y} - I_{x}\right)\omega_{x}\omega_{y} + \frac{1}{m_{p}}\left(k_{2}X - k_{3}Y\right) + k_{5}\left(\omega_{y}^{2} + \omega_{z}^{2}\right)\delta - k_{6}\omega_{y}\omega_{x}\delta + k_{7}\omega_{z}\dot{\delta}$$

$$g_{\delta} = \frac{k_{4}}{m_{p}}$$

$$(49)$$

with control input F_u corresponding to the servo actuator force. An appropriate sliding surface is designed in consideration of the desired actuator dynamics:

$$s_{\delta} = \dot{e}_{\delta} + k_1 e_{\delta} + k_2 \int_0^t e_{\delta} d\tau \tag{50}$$

where $e_{\delta} = \delta - \delta_c$ denotes displacement tracking error. k_1 and k_2 are the positive gains. By designing the appropriate k_1 and k_2 , the tracking error can obtain the desired dynamic characteristics.

Time differentiation of Equation (50) and substitution into Equation (48) yields:

$$\dot{s}_{\delta} = f_{\delta} + g_{\delta} F_{u} - \ddot{\delta}_{c} + k_{1} \dot{e}_{\delta} + k_{2} e_{\delta} \tag{51}$$

To mitigate chattering phenomena, an exponential reaching law [28] with boundary layer approximation is implemented:

$$F_{u} = g_{\delta}^{-1} \left(f_{\delta} - \ddot{\delta}_{c} + k_{1} \dot{e}_{\delta} + k_{2} e_{\delta} + c s_{\delta} + \varepsilon \cdot \operatorname{sat}(s_{\delta}) \right)$$
(52)

where c and ε are positive gains. $sat(\cdot)$ is a continuous function that can prevent the control chattering phenomenon.

$$sat(s_{\delta}) = \begin{cases}
-1 & s_{\delta} < -\Delta \\
\frac{s_{\delta}}{\Delta} & |s_{\delta}| \le \Delta \\
1 & s_{\delta} > \Delta
\end{cases}$$
(53)

with Δ defining the boundary layer thickness. Stability is guaranteed via the LaSalle-Yoshizawa theorem [29], ensuring the error state e_{δ} tends to zero as t tends to ∞ given proper gain selection k_1 and k_2 .

5. Simulation Results and Discussion

5.1. Simulation Scenarios and Uncertainties Configurations

The proposed control system was evaluated through Monte Carlo simulations encompassing 11 distinct scenarios (Table 1), designed to systematically assess performance under nominal and perturbed conditions. Key parameters of the hypersonic glider are summarized in Tables 2 and 3, with aerodynamic uncertainties modeled as uniformly distributed perturbations (±30% coefficients, ±20% inertia terms). Aerodynamic uncertainties include correlated variations in lift/drag coefficients per hypersonic similarity laws, we enforced: $\Delta C_x = 0.15 \times \Delta C_y^{\alpha} + 0.05 \times \left(\Delta C_y^{\alpha}\right)^2$ and $\Delta m_z^{\alpha} = -0.3 \times \Delta C_y^{\alpha}$. Parameter variations were sampled from Gaussian distributions $N(0, \sigma^2)$ with $\sigma = 30\%$ nominal, while preserving these physical constraints. The high dynamic pressure (814,000 Pa, Mach 10 at 15 kM) amplifies aerodynamic disturbances while reducing actuator effectiveness margins. Combined with strong inertia coupling, this creates a worst-case control scenario: lateral stability derivatives increase much than in subsonic regimes and control surfaces operate near saturation limits. These conditions validate the controller under extreme reentry stresses. Actuator constraints included saturation limits of ± 0.4 m for moving mass displacement and ± 5000 N for driving force. The BTT command consists of step inputs applied to the roll channel. We selected the controller gains through trial-and-error tuning as $k_{P1} = \text{diag}(3, 3)$, $k_{I1} = (0.25, 0.5)$, $k_{P2} = \text{diag}(2, 3.5)$, $k_1 = 6.4$, $k_2 = 16$, c = 25, $\varepsilon = 0.01$, and $\Delta = 0.01$. Adaptation update rate is selected T = 0.01s.

Table 1. Simulation scenarios.

Scenario Description	Abbreviation
Nominal conditions: dynamic inversion controller with no uncertainties	S1
Nominal conditions: L1 augmented controller with no uncertainties	S2
Dynamic inversion controller with reduced aileron functionality	S3
L1 augmented controller with reduced aileron functionality	S4
Dynamic inversion controller with aerodynamic uncertainties	S5
L1 augmented controller with aerodynamic uncertainties	S6
Dynamic inversion controller with high-frequency disturbances caused by the moving mass lateral movement	S7
L1 augmented controller with high-frequency disturbances caused by the moving mass lateral movement	S8
LQR controller with a combination of error(aileron, aerodynamic, moving mass lateral movement, gravimetric)	S9
Dynamic inversion controller with a combination of error(aileron, aerodynamic, moving mass lateral movement, gravimetric)	S10
L1 augmented controller with a combination of error(aileron, aerodynamic, moving mass lateral movement, gravimetric)	S11

Table 2. Parameters of Hypersonic Glider.

Symbol	Definition	Value
$\overline{I_z}$	Yaw inertia (principal)	$1200 \text{ kg} \cdot \text{m}^2$
$I_{\mathbf{z}}$	Pitch inertia (principal)	$1000 \text{ kg} \cdot \text{m}^2$
$I_{\mathbf{x}}$	Roll inertia (principal)	$400 \text{ kg} \cdot \text{m}^2$
I_{xy} , I_{xz} , I_{yz}	Products of inertia	$0 \text{ kg} \cdot \text{m}^2$
m_S	Total mass of system	1000 kg
μ	The moving mass ratio	0.1
S_B	Cross-sectional area	0.5 m^2
L	Reference length	4 m
Н	Flight height	15 km
v	Flight velocity	Ma = 10

Notation	Aircraft Equivalent	Value	Units	Physical Meaning
C_x	C_D	0.18		Drag
C_{y}^{α}	$\partial C_L/\partial \alpha$	3.2	$\rm rad^{-1}$	Lift curve slope
$C_y^{lpha} \ C_z^{eta}$	$\partial C_Y/\partial \beta$	-0.85	rad^{-1}	Sideforce slope
m_z^{α}	$\partial C_m/\partial \alpha$	-1.8	rad^{-1}	Pitch stability
$m_y^eta \ m_x^{\delta_a}$	$\partial C_n/\partial \beta$	0.16	rad^{-1}	Directional stability
$m_{\chi}^{\delta_a}$	$\partial C_l/\partial \delta_a$	0.038	${ m rad}^{-1}$	Primary roll control effectiveness
	$\partial C_L/\partial \delta_a$	0.0011	rad^{-1}	Lift change per aileron
	$\partial C_D/\partial \delta_a$	0.0003	rad^{-1}	Drag change per aileron
	$\partial C_m/\partial \delta_a$	0.0004	rad^{-1}	Pitching moment coupling
	$\partial C_Y/\partial \delta_a$	-0.0015	rad^{-1}	Sideforce coupling
	$\partial C_n/\partial \delta_a$	0.0009	rad^{-1}	Adverse yaw effect

Table 3. Controls-Neutral Aerodynamic Terms.

In addition, to demonstrate that the designed roll controller is robust to the high-frequency disturbances caused by the moving mass lateral movement, the movement of the moving mass is selected as Equation (54):

$$\delta = 0.1\sin(5\pi t) \quad (m), \quad t \ge 0 \tag{54}$$

5.2. Controller Performance Evaluation

(1) Nominal Conditions (Scenarios S1–S2)

Under nominal operating conditions (no uncertainties), both the dynamic inversion controller (S1) and L1-augmented (S2) controllers achieved effective roll-tracking. As illustrated in Figure 6, the settling time for a 10° roll step command was maintained below 1 s for both configurations, confirming baseline stability.

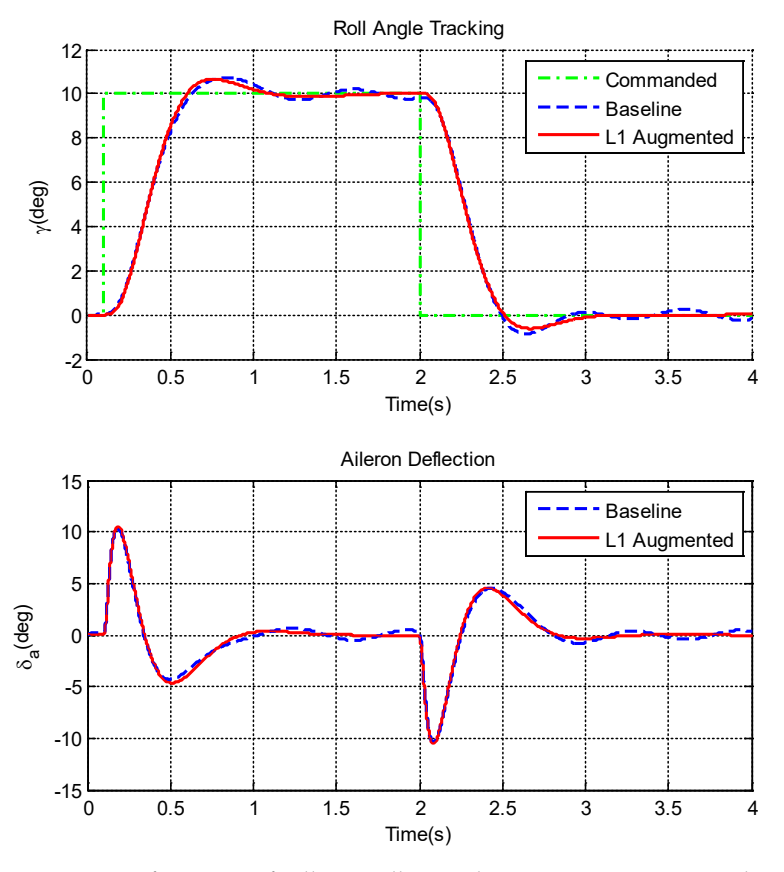


Figure 6. Performance of roll controllers with no uncertainties: S1 and S2.

(2) Actuator Impairment (Scenarios S3–S4)

Figure 7 demonstrates controller performance under 50% aileron authority reduction. The L1-augmented system (S4) exhibited a 14.69% lower tracking error than the baseline. This improvement is attributed to the adaptive controller's ability to compensate for reduced control effectiveness through uncertainty estimation.

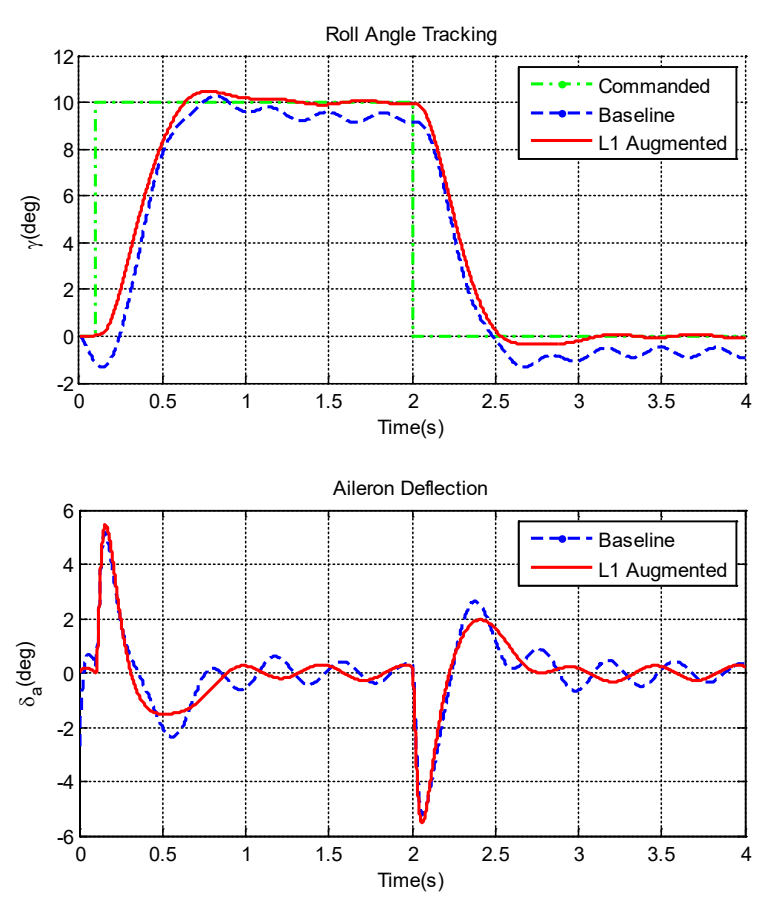


Figure 7. Performance of roll controllers with reduced aileron deflection: S3 and S4.

(3) Aerodynamic Uncertainties (Scenarios S5–S6)

With $\pm 30\%$ aerodynamic coefficient variations, the baseline dynamic inversion controller (S5) exhibited oscillatory behavior (peak-to-peak amplitude: 2.7°), as shown in Figure 8. In contrast, the L1-augmented controller (S6) suppressed oscillations by 72%, achieving less steady-state errors, underscoring the adaptive scheme's efficacy in handling parametric uncertainties.

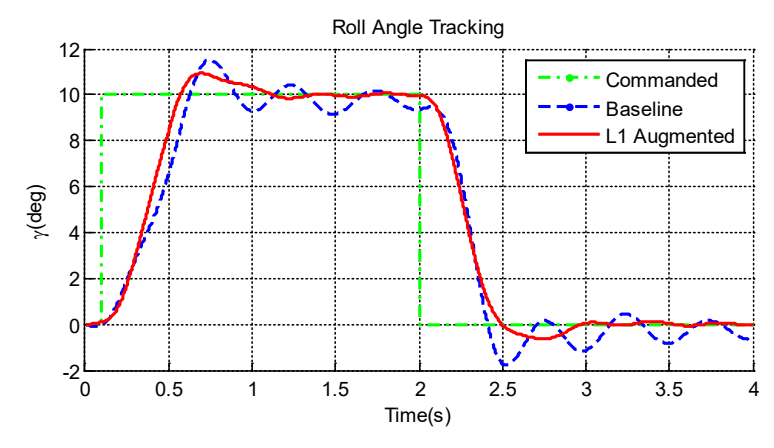


Figure 8. Cont.

Aerospace 2025, 12, 773 18 of 22

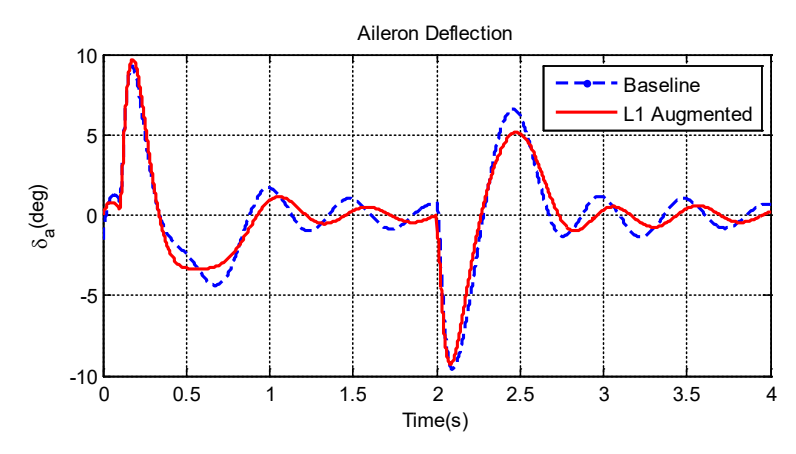


Figure 8. Performance of roll controllers with aerodynamic uncertainties: S5 and S6.

(4) High-Frequency Disturbances (Scenarios S7–S8)

Figure 9 presents the roll angle and the aileron deflection angle activity in the case that the actuator mass is moving by a high-frequency sinusoidal signal whose amplitude is 0.1 m. As shown from the simulation results, the steady-state error of roll angle has been significantly reduced once the L1 controller is used in the presence of the adverse effect caused by the high-frequency movement of the moving mass. The designed L1 adaptive controller can solve the problem of adaptive estimation and compensation for high-frequency disturbance, which cannot be solved by the conventional model reference adaptive control method.

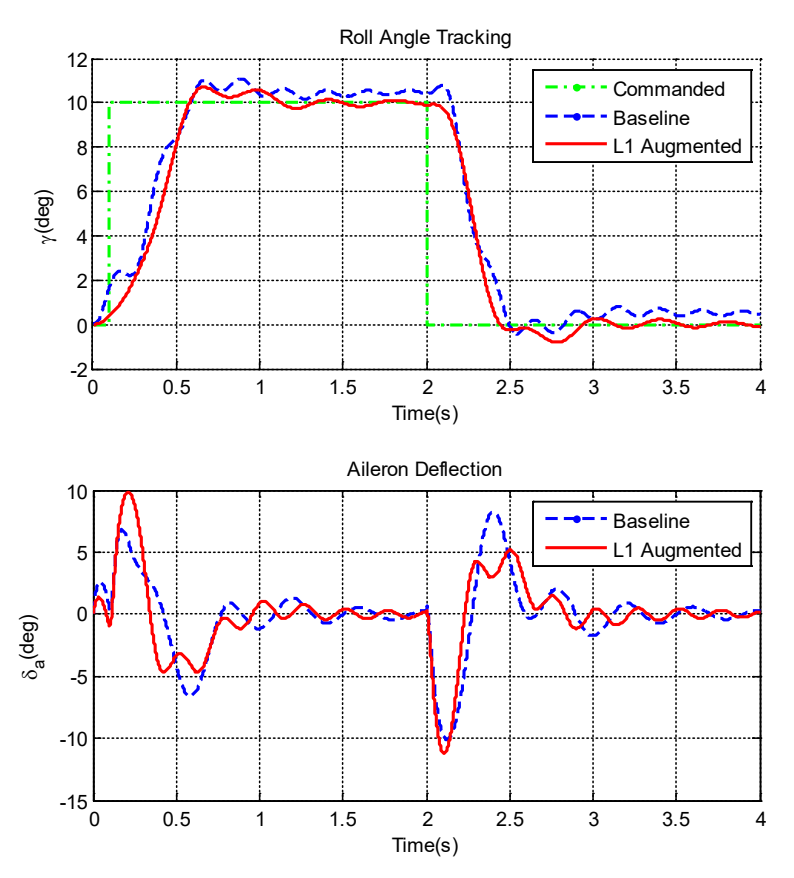


Figure 9. Performance of roll controllers with disturbances caused by the moving mass movement: S7 and S8.

(5) Combined Uncertainties (Scenarios S9–S11)

In order to demonstrate the usefulness and benefit of the proposed control system, the performance of the dynamic inversion baseline and the augmentation controllers is compared with that of a classic optimal controller by LQR methods [30]. Figure 10 depicts the performance in the presence of a combination of errors (S9, S10, and S11). As expected, the proposed control system could guarantee that the achieved angle tracks the commanded angle effectively. Compared with the LQR controller, a better tracking performance of the L1 augmented controller is achieved: small overshoot (nearly 10%), fast settling time (about 0.75 s), and small deviation from the commanded angle. The results show that the designed L1 adaptive controller displays a strong robustness for the parameter uncertainties, reduces aileron deflection, and the external high-frequency disturbance. The proposed control system can meet the requirements of fastness and robustness for a combination BTT control mode with a single moving mass and differential aileron.

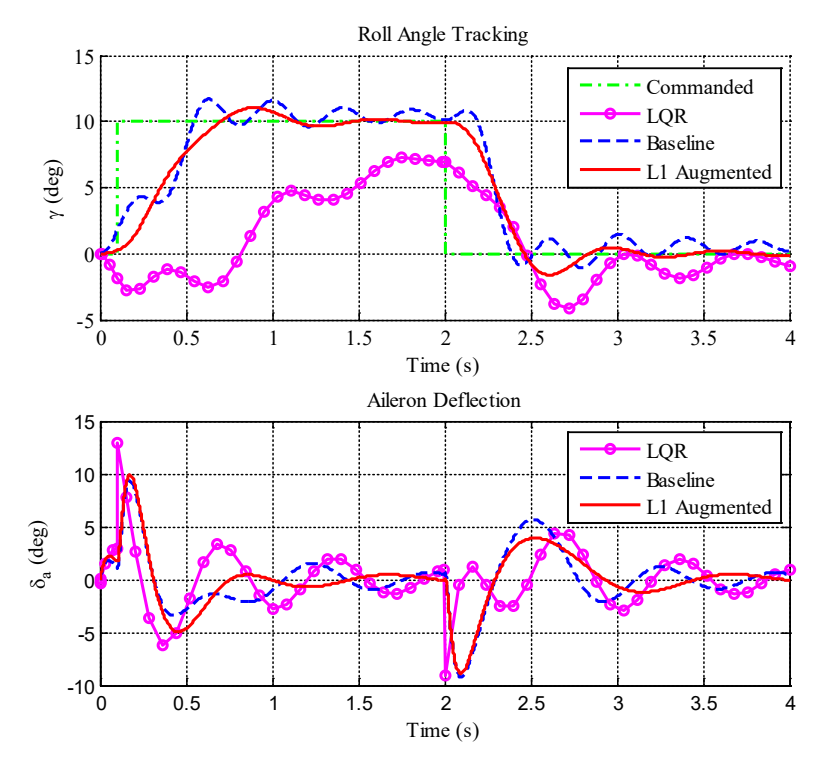


Figure 10. Performance of roll controllers with a combination of errors: S9, S11, and S10.

5.3. Robustness Analysis

The L_2 norm tracking error and time delay margin (TMD) constitute industry-standard metrics for flight control validation [27,31]: L_2 error integrates transient/steady-state performance [32] and TMD certifies robustness against real-world latency [31]. These metrics provide a complete characterization without redundancy.

(1) Tracking Error Metrics

The performance of the baseline and augmented controller can be compared by computing the L₂ norm of the tracking error e_p [32], which is defined as:

$$\|e_p\|_{L_2} = \sqrt{\int_0^T |e_p|^2 dt}$$
 (55)

The $\|e_p\|_{L_2}$ for simulation cases from the Monte Carlo runs are placed in Table 4.

Case	Baseline	Augmentation	Percentage Improvement, %
Nominal	9.32	8.81	5.44
Reduced aileron function	21.79	18.59	14.69
Aerodynamic uncertainties	15.46	13.10	15.27
Disturbances by moving mass	16.65	14.96	10.15
Combination	30.58	24.27	20.63

The following conclusions are drawn from Table 3. In the presence of reduced aileron functionality and aerodynamic uncertainties, the augmentation configuration greatly improves the performance of the baseline controller, especially in the case of aerodynamic uncertainties. The improvement of the performance of the baseline controller in the presence of the disturbances by moving mass with the L1 augmentation setup is weaker than other uncertainties. The L1 augmentation achieved maximum error reduction (20.63%) under combined uncertainties, demonstrating robust adaptation to worst-case perturbations.

(2) Robustness Analysis

For adaptive control, the time delay margin (TDM), which is defined as the maximum amount of time delay that the system can experience before instability occurs, is generally used as a robustness metric [31]. For this study, input delays have been added until the system shows signs of instability. The TDM results for the baseline and augmented controllers are placed in Table 5. As expected, the robustness margin of the adaptive controller is worse than the baseline controller as a result of the tradeoff between performance and robustness.

Table 5. Time delay margin.

Case	Baseline, ms	Augmentation, ms
Nominal	83	35
Reduced aileron function	112	58
Aerodynamic uncertainties	78	31
Disturbances by moving mass	97	49
Combination	123	72

Comparative Monte Carlo runs (500 independent vs. 500 correlated) reveal: L₂ tracking error: 24.27 \rightarrow 26.26 (+8.2%), TMD: 72 ms \rightarrow 69.8 ms (-3.1%). The controller maintains all performance metrics within $\pm 3\sigma$ bounds of nominal operation, confirming robustness against physical coupling.

6. Conclusions

This study establishes a novel bank-to-turn control paradigm for hypersonic reentry vehicles, integrating a single moving mass with differential ailerons to address aerodynamic ablation and structural complexity. The key theoretical and technical contributions are three-fold:

- 1. Coupled Dynamics Modeling: A 7-DOF inertial coupling model was derived, explicitly quantifying the interaction between moving mass displacement and roll-pitch dynamics. Stability criteria were analytically proven, defining critical roll rate thresholds to prevent divergence.
- 2. Hybrid Adaptive Control: A dynamic inversion baseline controller was augmented with an L1 adaptive architecture, achieving robust tracking under simultaneous parametric uncertainties ($\pm 30\%$ aerodynamics), actuator saturation (50% authority loss), and high-frequency disturbances (10 Hz). Monte Carlo simulations demonstrated a

Aerospace 2025, 12, 773 21 of 22

20.63% reduction in L2-norm tracking error under worst-case perturbations compared to dynamic inversion control.

3. Cross-Disciplinary Validation: The proposed configuration eliminated elevator/rudder ablation risks while maintaining sub-degree attitude precision, with performance metrics surpassing conventional LQR and MRAC approaches.

As a preliminary investigation, this work focused on rigid-body dynamics, omitting thermal ablation effects and flexible body interactions. Future research should prioritize: (1) Integrating ablation-induced mass loss and aerodynamic heating into the control framework. (2) Co-designing moving mass and aileron actuation for coupled pitch-roll-yaw maneuvers. (3) Implementing hardware-in-loop tests with hypersonic wind tunnel facilities to verify disturbance rejection capabilities. (4) Exploring neural-L1 hybrid controllers to further enhance robustness against stochastic hypersonic flow regimes.

These advancements will bridge the gap between theoretical control design and practical hypersonic vehicle deployment, offering a roadmap for next-generation reusable launch systems.

Author Contributions: Methodology and writing original draft preparation, P.W.; investigation and resources, writing—review and editing, P.C.; project administration and funding acquisition, C.G. All authors have read and agreed to the published version of the manuscript.

Funding: This research was funded by the National Natural Science Foundation of China (NNSFC) through Grant Nos. 11572097.

Data Availability Statement: Data are contained within the paper.

Conflicts of Interest: The authors declare no conflicts of interest.

References

- Meng, Q.K.; Yang, H.; Jiang, B. Fault-Tolerant Optimal Spacecraft Attitude Maneuver: An Incremental Model Approach. J. Guid. Control Dyn. 2022, 45, 1676–1691. [CrossRef]
- 2. Meng, Q.K.; Yang, H.; Jiang, B. Second-order sliding-mode on SO(3) and fault-tolerant spacecraft attitude control. *Automatica* **2023**, *149*, 110814. [CrossRef]
- 3. Sun, J.H.; Jing, W.X.; Chen, J. Robust Soft-Switching Multiple Model Predictive Control for Moving-Mass Reentry Vehicle. *J. Guid. Control Dyn.* **2024**, 47, 1488–1498. [CrossRef]
- 4. Yao, C.; Liu, Z.T.; Zhou, H.; Gao, C.S.; Li, J.Q.; Zhang, Z.M. Integrated guidance and control for underactuated fixed-trim moving mass flight vehicles. *Aerosp. Sci. Technol.* **2023**, *142*, 108680. [CrossRef]
- 5. Gu, Y.; Zhang, G.X.; Bi, Y.; Meng, W.Y.; Ma, X.P.; Ni, W.J. Pitch Mathematical Modeling and Dynamic Analysis of a HALE UAV with Moving Mass Control Technology. *Aerospace* **2023**, *10*, 918. [CrossRef]
- 6. Siling, W.; Sichen, J.; Yang, Z.; Hongyan, S. The modeling and cascade sliding mode control of a moving mass-actuated coaxial dual-rotor UAV. *Proc. Inst. Mech. Eng. Part G-J. Aerosp. Eng.* **2023**, 237, 3336–3351. [CrossRef]
- 7. Qiu, X.Q.; Gao, C.S.; Wang, K.F.; Jing, W.X. Attitude Control of a Moving Mass-Actuated UAV Based on Deep Reinforcement Learning. *J. Aerosp. Eng.* **2022**, *35*, 04021133. [CrossRef]
- 8. Hu, Y.D.; Lu, Z.L.; Ling, K.V.; Liao, W.H.; Zhang, X. Multiplexed MPC attitude control of a moving mass satellite using dual-rate piecewise affine model. *Aerosp. Sci. Technol.* **2022**, 128, 107778. [CrossRef]
- 9. Sun, J.H.; Jing, W.X.; Gao, C.S.; Wu, T. Attitude dynamics and control of high-mass-ratio fixed-trim moving mass reentry vehicle. *Aerosp. Sci. Technol.* **2022**, 123, 107456. [CrossRef]
- 10. Dong, K.X.; Zhou, J.; Zhou, M.; Zhao, B. Roll control for single moving-mass actuated fixed-trim reentry vehicle considering full state constraints. *Aerosp. Sci. Technol.* **2019**, *94*, 105365. [CrossRef]
- 11. Li, G.L.; Yang, M.; Wang, S.Y.; Chao, T. Modified rolling guidance law for single moving mass controlled reentry vehicle against maneuvering target with impact angle constraints. *Chin. J. Aeronaut.* **2022**, *35*, 226–239. [CrossRef]
- 12. Frost, G.; Costello, M. Linear theory of a rotating internal part projectile configuration in atmospheric flight. *J. Guid. Control Dyn.* **2004**, 27, 898–906. [CrossRef]
- 13. Li, J.Q.; Gao, C.S.; Jing, W.X.; Wei, P.X. Dynamic analysis and control of novel moving mass flight vehicle. *Acta Astronaut*. **2017**, 131, 36–44. [CrossRef]

Aerospace 2025, 12, 773 22 of 22

14. Menon, P.K.; Sweriduk, G.D.; Ohlmeyer, E.J.; Malyevac, D.S. Integrated guidance and control of moving-mass actuated kinetic warheads. *J. Guid. Control Dyn.* **2004**, *27*, 118–126. [CrossRef]

- 15. Chattopadhyay, S.; Sukumar, S.; Natarajan, V. Model reference adaptive control for state and input constrained linear systems. *Eur. J. Control* **2025**, *82*, 101196. [CrossRef]
- 16. Mohseni, N.; Bernstein, D.S. Retrospective-cost-based model reference adaptive control of nonminimum-phase systems. *Int. J. Adapt. Control Signal Process.* **2024**, *38*, 2404–2422. [CrossRef]
- 17. Wu, Z.H.; Cheng, S.; Zhao, P.; Gahlawat, A.; Ackerman, K.A.; Lakshmanan, A.; Yang, C.Y.; Yu, J.H.; Hovakimyan, N. L1 Quad: L1 Adaptive Augmentation of Geometric Control for Agile Quadrotors With Performance Guarantees. *IEEE Trans. Control Syst. Technol.* 2025, 33, 597–612. [CrossRef]
- 18. Ma, T.; Cao, C.Y. L1 adaptive output-feedback control of multivariable nonlinear systems subject to constraints using online optimization. *Int. J. Robust Nonlinear Control* **2019**, 29, 4116–4134. [CrossRef]
- 19. Hovakimyan, N.; Cao, C.Y.; Kharisov, E.; Xargay, E.; Gregory, I.M. L1 Adaptive Control for Safety-Critical Systems Guaranteed Robustness with Fast Adaptation. *IEEE Control Syst. Mag.* **2011**, *31*, 54–104. [CrossRef]
- 20. Khankalantary, S.; Ahvanouee, H.R.; Mohammadkhani, H. L1 Adaptive integrated guidance and control for flexible hypersonic flight vehicle in the presence of dynamic uncertainties. *Proc. Inst. Mech. Eng. Part I-J. Syst. Control Eng.* **2021**, 235, 1521–1531. [CrossRef]
- Wang, J.; Holzapfel, F.; Xargay, E. Non-cascaded Dynamic Inversion Design for Quadrotor Position Control with L 1 Augmentation. In Proceedings of the 2nd CEAS Specialist Conference on Guidance, Navigation and Control, Delft, The Neterlands, 10–12 April 2013; pp. 291–310.
- 22. Leman, T.J. L1 adaptive control augmentation system for the X-48B Aircraft. In Proceedings of the AIAA Guidance, Navigation, and Control Conference, Chicago, IL, USA, 10–13 August 2009.
- 23. Banerjee, S.; Wang, Z.J.; Baur, B.; Holzapfel, F.; Che, J.X.; Cao, C.Y. L1 Adaptive Control Augmentation for the Longitudinal Dynamics of a Hypersonic Glider. *J. Guid. Control Dyn.* **2016**, *39*, 275–291. [CrossRef]
- 24. Phillips, W.H. Effect of Steady Rolling on Longitudinal and Directional Stability; Technical Report Archive & Image Library; Langley Memorial Aeronautical Laboratory: Hampton, VA, USA, 1948.
- 25. Singh, S.N.; Steinberg, M.L.; Page, A.B. Nonlinear adaptive and sliding mode flight path control of F/A-18 model. *IEEE Trans. Aerosp. Electron. Syst.* **2003**, 39, 1250–1262. [CrossRef]
- 26. Lu, X.Y.; Hedrick, J.K. Integral filters from a new viewpoint and their application in nonlinear control design. In Proceedings of the Joint 2000 Conference on Control Applications and Computer-Aided Control Systems Design Symposium, Anchorage, Alaska, 25–27 September 2000; pp. 501–506.
- 27. Hovakimyan, N.; Cao, C. L1 Adaptive Control Theory; SIAM: Philadelphia, PA, USA, 2010.
- 28. Lee, K.W.; Nambisan, P.R.; Singh, S.N. Adaptive variable structure control of aircraft with an unknown high-frequency gain matrix. *J. Guid. Control Dyn.* **2008**, *31*, 194–203. [CrossRef]
- 29. Krastic, B.M.; Kanellakopolous, I.; Kokotovic, V.P. Nonlinear and Adaptive Control Design; Wiely: New York, NY, USA, 1995.
- Mracek, C.P.; Ridgely, D.B. Missile Longitudinal Autopilots: Connections Between Optimal Control and Classical Topologies. In Proceedings of the AIAA Guidance, Navigation, and Control Conference and Exhibit, San Francisco, CA, USA, 15–18 August 2005.
- 31. Dorobantu, A.; Seiler, P.; Balas, G.J. Time-Delay Margin Analysis for an Adaptive Controller. *J. Guid. Control Dyn.* **2015**, 35, 1418–1425. [CrossRef]
- 32. Heise, C.D.; Leitao, M.; Holzapfel, F. Performance and Robustness Metrics for Adaptive Flight Control-Available Approaches. In Proceedings of the AIAA Guidance, Navigation, and Control (GNC) Conference, Boston, MA, USA, 19–22 August 2013.

Disclaimer/Publisher's Note: The statements, opinions and data contained in all publications are solely those of the individual author(s) and contributor(s) and not of MDPI and/or the editor(s). MDPI and/or the editor(s) disclaim responsibility for any injury to people or property resulting from any ideas, methods, instructions or products referred to in the content.